JOURNAL OF GEOPHYSICAL RESEARCH, VOL. 107, NO. D19, 4364, doi:10.1029/2001JD001491, 2002

Impact of satellite-derived effective cloud fraction on calculated actinic flux, photodissociation rates, and OH production

O. N. E. Tuinder, R. de Winter-Sorkina,[1] and P. J. H. Builtjes[2]

Institute for Marine and Atmospheric Research Utrecht, Utrecht University, Utrecht, Netherlands

Received 13 November 2001; revised 18 February 2002; accepted 28 February 2002; published 1 October 2002.

[1] Clouds are a large error source in the retrieval of tropospheric column densities and concentration profiles of trace gas species from satellites and in the calculation of their photodissociation rates. The Global Ozone Monitoring Experiment instrument on the ERS-2 satellite is capable of detecting clouds, and a number of methods have been developed to retrieve their properties. In our previous study it was shown that these cloud retrieval methods calculate an effective cloud fraction that is related to a cloud with a high optical thickness. Furthermore, the retrieved solutions are nonunique, as different combinations of optical thickness, cloud fraction, and cloud top height can give the same albedo at the top of the atmosphere. The impact of the scaling of various cloud solutions to an effective cloud fraction on the vertical photodissociation profiles of ozone (O_3) and nitrogen dioxide (NO_2) and on the tropospheric column production of the hydroxyl radical (OH) is studied in this paper, using the tropospheric ultraviolet-visible radiative transfer model. Results show that for selected cloud solutions, local differences in the vertical OH primary production profile can be from +7% for small solar zenith angles to −14% for large angles with a cloud between 2 and 3 km. Column-integrated OH primary production differences can be between +9% and −7% depending on the solar zenith angle when a cloud is located between 2 and 3 km but can increase to +23% and −81% for a cloud at higher altitudes. NO_2 photodissociation was shown to be locally more influenced by the scaling of clouds to an effective cloud fraction, but for the tropospheric column difference this influence is less prominent. *INDEX TERMS:* 0320 Atmospheric Composition and Structure: Cloud physics and chemistry; 3359 Meteorology and Atmospheric Dynamics: Radiative processes; 3360 Meteorology and Atmospheric Dynamics: Remote sensing; *KEYWORDS:* remote sensing, cloud fraction, actinic flux, photodissociation, OH

Citation: Tuinder O. N. E., R. de Winter-Sorkina, and P. J. H. Builtjes, Impact of satellite-derived effective cloud fraction on calculated actinic flux, photodissociation rates, and OH production, *J. Geophys. Res.*, *107*(D19), 4364, doi:10.1029/2001JD001491, 2002.

1. Introduction

[2] Photodissociation of trace gases by solar radiation is an important topic in atmospheric chemistry studies. For a number of atmospheric constituents the destruction by absorption of high energetic photons can be a significant local sink, and often the highly reactive dissociation products initiate production of other species which play a role in various atmospheric chemistry processes. A number of well-known trace gases that photodissociate under influence of ultraviolet (UV) light are ozone, nitrogen dioxide, formaldehyde, and acetaldehyde.

[3] Photodissociation of ozone (O_3) produces an exited oxygen atom which can produce hydroxyl radicals (OH) in a subsequent reaction with water vapor in an unpolluted environment (equation (1)). This way of OH production is called primary production. The exited oxygen atom can also collide with one of the abundant air molecules, which reduces its excitation state.

$$O_3 + h\nu \xrightarrow{j(O_3)} O_2(^1\Delta_g) + O(^1D) \quad (1a)$$

$$O(^1D) + H_2O \xrightarrow{k_1} 2OH \quad (1b)$$

$$O(^1D) + N_2 \xrightarrow{k_2} O(^3P) + N_2 \quad (1c)$$

$$O(^1D) + O_2 \xrightarrow{k_3} O(^3P) + O_2. \quad (1d)$$

Here the photolysis frequency (s^{-1}) is denoted as j and k_x (cm^3 $molecule^{-1}$ s^{-1}) are chemical reaction constants (provided in Table 1).

[4] Hydroxyl is an extremely reactive species, and it determines, for a large part, the oxidizing capacity of the

[1] Currently at National Institute of Public Health and the Environment, Bilthoven, Netherlands.

[2] Also at Netherlands Organization for Applied Scientific Research, Institute of Environmental Sciences, Energy, and Process Innovation, Apeldoorn, Netherlands.

0148-0227/02/2001JD001491

Table 1. Reaction Constants Used for Equations (1), (2), and (7)[a]

k Factor	Value	Unit
k_1 H_2O[b]	2.2×10^{-10}	cm^3 $molecule^{-1}$ s^{-1}
k_2 N_2[c]	$1.8 \times 10^{-11} \times e^{(107/T)}$	cm^3 $molecule^{-1}$ s^{-1}
k_3 O_2[c]	$3.2 \times 10^{-11} \times e^{(67/T)}$	cm^3 $molecule^{-1}$ s^{-1}
k_4 $O(^3P) + O_2 + M$[b]	6.0×10^{-34} $(T/300)^{-2.3}$	cm^6 $molecule^{-2}$ s^{-1}
k_5 $NO + HO_2$[b]	$3.0 \times 10^{-12} e^{(250/T)}$	cm^3 $molecule^{-1}$ s^{-1}

[a] Temperature (T) is in degrees Kelvin.
[b] From *Sander et al.* [2000].
[c] From *Warneck* [1988].

atmosphere. The inclusion of hydroxyl in chemical models has better explained the lifetime of carbon monoxide, methane, and other long-living species [*Levy*, 1971; *Warneck*, 1988; *Seinfeld and Pandis*, 1998].

[5] In polluted environments with high NO_x concentrations the photodissociation of nitrogen dioxide (NO_2) is also important because via its dissociation products it is responsible for major local O_3 production:

$$NO_2 + h\nu \xrightarrow{j(NO_2)} NO + O(^3P) \quad (2a)$$

$$O(^3P) + O_2 + M \xrightarrow{k_4} O_3 + M \quad (2b)$$

$$NO + HO_2 \xrightarrow{k_5} NO_2 + OH. \quad (2c)$$

[6] Box model studies estimating the contributions to the daily integrated OH production in different regimes have shown that at surface level, production of OH by photolysis of O_3 accounts for 76% of the total in unpolluted oceanic regimes, 44% in rural regimes, and 25% in polluted regimes, where production of OH via a reaction of NO + HO_2 is 9%, 42%, and 71%, respectively [*van Weele*, 1997]. This indicates that for unpolluted areas the primary production dominates and in polluted regimes the NO_x reactions. Three-dimensional global model simulations show that for averaged global tropospheric OH, typically twice as much primary production is found than recycling production [*van Weele*, 1997].

[7] Because of the high reactivity of OH and thus the short lifetime, in the order of a few seconds, the concentration is low, and in situ concentration measurements are relatively difficult to perform and include long path length differential absorption measurements, laser-induced fluorescence measurements or chemical conversion, and measurement of the resulting product [*Mount*, 1992; *Hard et al.*, 1984; *Eisele and Tanner*, 1991]. On the other hand, global model studies are performed where OH calculations are optimized by fitting the modeled methyl-chloroform concentrations to the measured ones at Atmospheric Lifetime Experiment/Global Atmosphere Gases Experiment/Advanced Global Atmosphere Gases Experiment stations [*Prinn et al.*, 1995; *Krol et al.*, 1998]. From these model studies, trends in OH concentrations over the past few decades were deduced, and the value and direction of the trends has been subject of discussion in the literature [*Prinn and Huang*, 2001; *Krol et al.*, 2001; *Prinn et al.*, 2001].

[8] Alternative to the use of in situ measurements and model studies, remote sensing techniques from space can be used for an indirect determination of OH primary production when actinic flux profiles are calculated and profiles of O_3 and H_2O are retrieved [*de Winter-Sorkina and Tuinder*, 1999; *de Winter-Sorkina*, 2000]. In this way, satellite data can provide additional independent information on global OH trends when several years of data are processed.

[9] The amount of light is a critical factor in photodissociation. Especially in the lower troposphere, clouds are a major factor in the radiation budget, and the photodissociation of molecules is highly influenced by their presence or absence. The scattering of light at a cloud layer can increase the diffuse backscattered radiation above and in the cloud layer and at the same time shield the layers below from the strong direct component of sunlight, leading to significant differences in the actinic flux [*van Weele and Duynkerke*, 1993; *Los et al.*, 1997].

[10] Modern satellite instruments such as the nadir-viewing Global Ozone Monitoring Experiment instrument (GOME) on board the ERS-2 have provided a constant flow of data with a high spectral resolution and a full geographical coverage. This type of data is used for retrieval of density columns of atmospheric constituents such as NO_2, BrO, SO_2, OClO, and HCHO [*Burrows et al.*, 1999]; H_2O [*Maurellis et al.*, 2000; *Noel et al.*, 1999; *Casadio et al.*, 2000]; and retrieval of vertical profiles of O_3 [*van der A et al.*, 1998; *Munro et al.*, 1998; *Hoogen et al.*, 1999]. From the same data, cloud properties can be calculated by various methods. The combination of trace gas measurements with cloud information from the same satellite gives an advantage with respect to colocation and timing of data than when a separate source of cloud information is used. The SCIAMACHY instrument on board ENVISAT will additionally measure CH_4 and CO, which are the main sinks for OH.

[11] In a previous study [*Tuinder et al.*, 2002], four cloud detection methods for GOME were reviewed and compared with synoptic observations: Initial Cloud Fitting Algorithm (ICFA) [*Kuze and Chance*, 1994], PMD Cloud Recognition Algorithm (PCRA)/Cloud Retrieval Algorithm for GOME (CRAG) [*Kurosu et al.*, 1999], Optical Cloud Recognition Algorithm (OCRA) [*Loyola*, 1998; *von Bargen et al.*, 2000], and Fast Retrieval Scheme for Clouds from the Oxygen-A Band (FRESCO) [*Koelemeijer and Stammes*, 2001]. In this study, a separation of colocated synoptically observed clouds and satellite-retrieved clouds by observed optical thickness showed that synoptical clouds with a small optical thickness and a large fractional cover are represented by the satellite retrieval methods as optically thick clouds with a small cloud fraction. This means that only an effective value for the cloud fraction is retrieved. Of the four methods, the authors found the FRESCO method the most promising because it retrieved the cloud fraction and the cloud top height at the same time while the ICFA used International Satellite Cloud Climatology Project climatological data for cloud top heights and PCRA/CRAG needed two separate steps to retrieve the cloud top.

[12] In studies by *Kuze and Chance* [1994] and *Koelemeijer and Stammes* [1999, 2001] it is shown that the same radiation at the top of the atmosphere (TOA) can be attained by different combinations of cloud fraction, cloud optical thickness, and cloud top height when other factors such as the surface albedo are known. An example of this situation is shown in Figure 1, where a cloud with a low optical

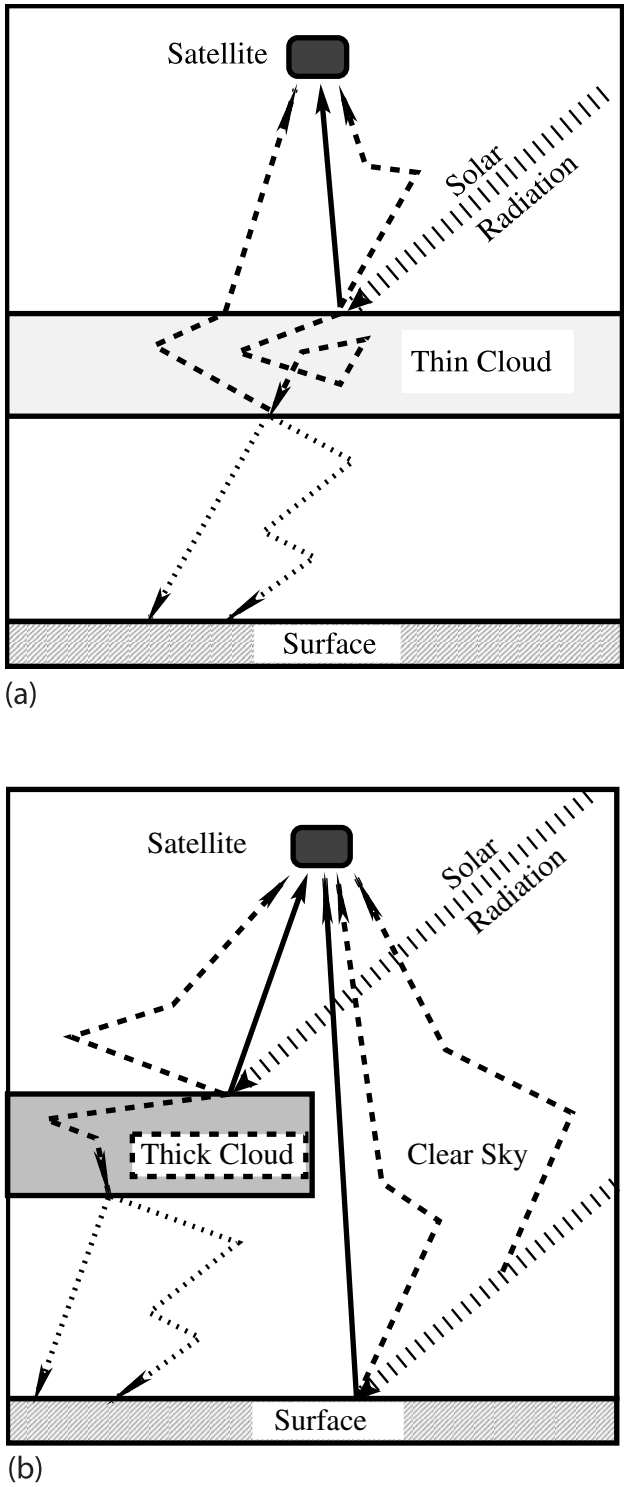

Figure 1. Radiative transfer in (a) a case where the optical thickness is low combined with a complete cloud cover and (b) a case where the optical thickness is high with a partially covered sky.

thickness and a complete cover gives the same radiation at TOA as the case where a cloud with a higher optical thickness, with a relatively higher reflectivity, and a partial cover is present.

[13] In *von Bargen et al.* [2000] and *Koelemeijer and Stammes* [2001] it was shown that the cloud top height can be estimated by analysis of O_2-A band absorption in the GOME data. This reduces the free parameters to the optical thickness τ and the cloud fraction f.

[14] The consequences of the scaling of the cloud characteristics to an effective thick cloud giving different cloud solutions (fractional cover, optical thickness) for different cloud altitudes on the UV actinic flux profiles and thus on the photodissociation and finally on the difference in primary OH production is the subject of this current study. In this paper, section 2 gives an overview of the radiative transfer aspects of photodissociation, section 3 gives a description of the methods and model used, and in section 4 the results will be presented and discussed. Section 5 is for conclusions.

2. Photodissociation

[15] In this section we will describe how we calculate the photolysis rates and discuss other issues that are important for our radiative transfer calculations with atmospheres containing clouds. The theory of radiative transfer is extensively discussed in various works like *Liou* [1980], *Goody and Yung* [1989], and *Liou* [1992], so we will only mention the essential parameters here.

[16] To calculate transmittance or reflectance at a point in a nonabsorbing atmosphere, one needs to know the atmospheric structure, consisting of air pressure profiles for Rayleigh scattering, aerosol load profiles τ_{aer}, and information about clouds (optical thickness τ_{cloud}, cloud top h_t and bottom h_b, and assumed cloud particle shape and size distribution or parameterizations thereof) for Mie scattering. Further information on the solar radiation at the TOA and the solar zenith angle (SZA) then enables us to calculate actual fluxes. In an absorbing atmosphere, information on absorption cross sections and concentration profiles of important species also need to be known, i.e., O_3 and NO_2 in our case.

[17] The monochromatic actinic flux F (W m^{-2} nm^{-1}) at a point is defined as the spherically integrated incident monochromatic radiance I (W m^{-2} nm^{-1} sr^{-1}) (equation (3)). This includes both the direct radiation and the diffuse radiation.

$$F = \int_{4\pi} I \, d\Omega. \tag{3}$$

[18] Assuming homogeneous clouds of the same cloud type, the radiation in an atmosphere with broken clouds can be separated into a clouded part and a clear sky part, proportional to the cloud fraction f_c (the weighted plane parallel approach, see *Cahalan et al.* [1994]). The actinic flux in a fractional clouded situation then becomes (equation (4)):

$$F = F_{\text{cloud}} \times f_c + F_{\text{clear}} \times (1 - f_c), \tag{4}$$

where F_{cloud} and F_{clear} are the local actinic fluxes for a completely clouded and clear situation, respectively. One of the reasons to use this weighted plane parallel approach is the large size of a GOME pixel: 320 $\times$ 40 km^2. This is large enough to avoid significant exchange between the clear part

and the clouded part in the calculation of the radiances [*Marshak et al.*, 1995].

[19] The photolysis frequency j (s^{-1}) of a species x is defined as the integral over wavelength λ (nm) of the absorption cross section σ_x (m^2) times the quantum yield ϕ_x (J^{-1}) times the actinic flux F (equation (5)). The quantum yield and the absorption cross section are wavelength and temperature dependent.

$$j_x = \int_\lambda \sigma_x(\lambda, T)\ \phi_x(\lambda, T)\ F(\lambda)\ d\lambda. \quad (5)$$

[20] The local primary production rate P_0 ($cm^{-3}\ s^{-1}$) of OH is determined by the number density of ozone (O_3) (cm^{-3}), water vapor number density (H_2O), and the photolysis frequency j of ozone:

$$P_0(\mathrm{OH}) = 2 \times f_{\mathrm{H_2O}} \times j_{\mathrm{O_3}} \times [\mathrm{O_3}], \quad (6)$$

where f_{H_2O} denotes the branching ratio of $O(^1D)$ between reactions with N_2, O_2, and water vapor molecules:

$$f_{\mathrm{H_2O}} = k_1 \times [\mathrm{H_2O}]/(k_1 \times [\mathrm{H_2O}] + k_2 \times [\mathrm{N_2}] + k_3 \times [\mathrm{O_2}].) \quad (7)$$

Factors k_x denote the temperature-dependent reaction constants for species x.

3. Radiative Transfer Model

3.1. Model Description

[21] The radiative transfer model used for this study is the tropospheric ultraviolet-visible (TUV) radiation model version 4.1a from *Madronich and Flocke* [1998]. The model was set up to use the discrete ordinates radiative transfer algorithm with eight streams [*Stamnes et al.*, 1988] in a plane-parallel atmosphere with 121 levels: from 0 to 10 km in steps of 200 m and from 11 to 80 km in steps of 1 km. Atmospheric constituent profiles of O_2, N_2, O_3, NO_2, H_2O, and temperature profiles for midlatitude summer from Air Force Geophysics Laboratory were used [*Anderson et al.*, 1986] to calculate the Rayleigh scattering, ozone, and NO_2 absorption and also as input profiles for the reaction of $O(^1D)$ with H_2O to produce OH. The total ozone column was set to 300 Dobson units (1 DU = 0.001 atm cm).

[22] Quantum yields from *Sander et al.* [2000] determined the photodissociation of O_3 and the quantum yields for NO_2 were taken from *Gardner et al.* [1987]. Calculations were performed from 150 to 425 nm in 1 nm wide steps, which includes the complete photodissociation range of O_3 and NO_2. *Madronich and Weller* [1990] have shown that a 1 nm resolution keeps the numerical calculation error of O_3 and NO_2 photodissociation within 1% of calculations with a higher wavelength resolution.

[23] For cases with clouds a horizontally and vertically homogeneous cloud with a prescribed total optical thickness τ, between altitudes h_b and h_t, with a Henyey-Greenstein scattering phase function, asymmetry factor $g = 0.875$, and a single scattering albedo $\omega = 0.9999$ was inserted in the lower part of the model atmosphere. The TUV model automatically divides the cloud into layers of equal optical thickness using the standard levels provided by the model. Calculations for situations with fractional cloud cover used the approach in equation (4).

[24] The surface albedo A_s was fixed to 0.05 for all situations. The TUV default aerosol profile that contributes to the scattering and absorption ($\omega = 0.99$) from the surface to 50 km was taken from *Elterman* [1968], which corresponds to a column aerosol optical thickness of $\tau = 0.38$ at $\lambda = 340$ nm. Also, the default solar spectrum in the TUV model was used with an Earth-sun distance of 1 AU at the spring equinox.

3.2. Error Sources

[25] In the model description in section 3.1 the information to calculate actinic flux, photodissociation rates, and OH primary production in the troposphere is given. In practice, water vapor has been proven to be a very important factor when calculating OH primary production. Its local concentration (specific humidity) can vary by 2 orders of magnitude depending on the location on Earth (and altitude) and has, via the branching ratio (equation (7)), a large impact on the local production. Fortunately, most of the water vapor is concentrated in the relatively well-mixed lower part of the troposphere. Retrieval of total water vapor columns from GOME satellite data is possible and has an error of ~18% compared with Solar Maximum Misson I if an appropriate reference atmosphere is taken (based on, e.g., latitude, as in our model) [*Noel et al.*, 1999]. Water vapor profiles from the European Centre for Medium-Range Weather Forecasting (ECMWF) can also be used for calculating the OH primary production.

[26] The sensitivity for ozone can be divided into two parts: the sensitivity of OH production to the tropospheric ozone profile and the sensitivity of the actinic flux, photodissociation rates, and OH production to the total ozone column. If the ozone concentration is only increased locally, then the local OH production will also increase locally with roughly the same factor. The tropospheric ozone profiles can be retrieved from GOME measurements with an accuracy better than 40% [*Siddans et al.*, 1999].

[27] However, if all the concentrations in a column are increased, then the effect of more available ozone for photodissociation is canceled by the reduced UV flux by the greater absorption of UV radiation by all the ozone in the stratosphere overhead (where most of the ozone is concentrated). Calculations with the TUV model show that an increase of the ozone column of 1 DU causes a decrease in OH production of 0.07% at the surface to 0.15% at higher altitudes in the troposphere. The currently retrieved total ozone columns from GOME have an accuracy better than 4% for a solar zenith angle (SZA) below 70° but can range between 4 and 10% for SZA between 70° and 85°, depending on the season [*Lambert et al.*, 2000]. Stratospheric profiles can be retrieved from GOME measurements with an accuracy better than 10% [*Munro et al.*, 1998; *Siddans et al.*, 1999].

[28] The impact of the clouds on OH production is the subject of this present study. An error in the cloud retrieval is difficult to give as an objective number. If the retrieved effective FRESCO cloud fraction is compared with averaged synoptically observed clouds in the same pixel, the average difference can be up to 20% [*Tuinder et al.*, 2002] because the observer on the ground separates between cloud fraction and cloud type while the retrieval method only

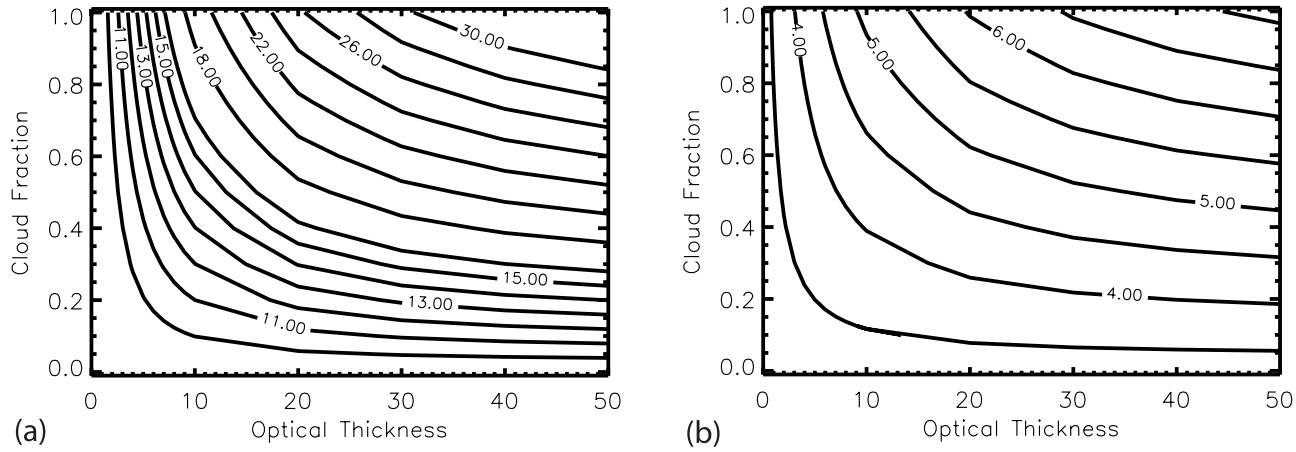

Figure 2. Upward wavelength integrated radiances from nadir (W m^{-2} sr^{-1}) at the top of the atmosphere for solar zenith angles: (left) 0° and (right) 75°. The radiances are integrated between 150 and 425 nm and the cloud is located between 2 and 3 km.

looks at the radiation. However, if FRESCO is compared with other satellite data, such as those from Along-Track Scanning Radiometer 2, having a high spatial resolution of 1 km × 1 km, the average difference in the effective cloud fraction is 0.04 [*Koelemeijer and Stammes*, 2001].

[29] The TUV model was run with plane-parallel clouds. This introduces an error in the calculation of actinic fluxes compared with a full Monte Carlo model taking into account the inhomogeneities in clouds. *Los et al.* [1997] calculated actinic fluxes in broken cloud fields at various degrees of cloudiness with a Monte Carlo model having a hexagonal cloud geometry. They give the actinic flux enhancement obtained with the doubling-adding radiative transfer algorithm for overcast conditions, which agrees very well with Monte Carlo simulations. From these data we estimated a plane-parallel bias for actinic flux at cloud top of 4% for 70% and 30% cloudiness, at cloud base of 4.5% for 70% cloudiness, and of 10% for 30% cloudiness (for a cloud optical thickness of $\tau = 20$ and a solar zenith angle of 0°).

4. Results and Discussion

4.1. Radiances at the Top of the Atmosphere

[30] As discussed in the introduction of this paper the amount of upward radiation at TOA is dependent on the combinations of optical thickness τ, cloud fraction f_c, and cloud top height h_t. We assume that the SZA is known (from the geographical location and date/time) and that the cloud top height was determined in a retrieval of the cloud properties. This leaves combinations of (τ, f_c) as the only two free parameters describing the clouds.

[31] In order to select possible solutions for (τ, f_c), the upward wavelength integrated radiance I^* (W m^{-2} sr^{-1}) from nadir at TOA between 150 and 425 nm for combinations of optical thickness and cloud fraction was calculated and is shown in Figure 2. Following an isoline of I^*, solutions for (τ, f_c) at a fixed cloud altitude and SZA can be determined at regular cloud fraction intervals. These sets of (τ, f_c) for a number of cases are provided in Table 2.

[32] The starting point for the solution sets is ($\tau = 2.0$, $f_c = 1.0$), and the other combinations follow with steps of $\Delta f_c = 0.2$ to $f_c = 0.2$, then $f_c = 0.1$, and the last combination is defined by optical thickness $\tau = 50$ with the appropriate cloud fraction denoted by f_c^*.

[33] Both Figure 2 and Table 2 show that for large cloud fractions, only a small increase in cloud optical thickness is needed for the cloud fraction decrease $\Delta f_c = 0.2$, while at lower cloud fractions the increase in optical thickness is considerably larger. This is due to the saturation in reflectance that occurs with increasing optical thickness, together with a decreasing cloud fraction in the (τ, f_c) combination.

[34] The radiation at TOA is also decreasing with increasing SZA for the same combination of (τ, f_c). For example, the upward wavelength integrated radiance I^* at ($\tau = 2.0$, $f_c = 1.0$) drops from 11.46 W m^{-2} sr^{-1} for SZA = 0° to 3.93 W m^{-2} sr^{-1} for SZA = 75° and a cloud between 2 and 3 km.

4.2. Actinic Flux Profiles and OH Production

[35] For the combinations of (τ, f_c) that give 11.46 W m^{-2} sr^{-1} of radiation between 150 and 425 nm at TOA with a cloud between 2 and 3 km and SZA = 0° (case a), several calculations were made. First profiles of the actinic flux and the photodissociation frequency of O_3 were calculated, then the production of $O(^1D)$ was determined (Figure 3). From the $O(^1D)$ production the OH production was calculated, and finally the production difference relative to the reference thick cloud combination ($\tau = 50$, f_c^*) of OH was calculated (Figure 4). Owing to space constraints, we only provide individual plots for cases a and d, and we will mention the results of the other cases in the text.

Table 2. Combination of Optical Thickness τ, Cloud Fraction f_c, and Cloud Bottom and Top h for the Same Wavelength-Integrated Upward Radiance I^* at TOA (W m^{-2} sr^{-1}) ($\lambda = 150-425$ nm) at a Fixed SZA θ_0

Case	θ_0	I^*	h, km	f_c	1.0	0.8	0.6	0.4	0.2	0.1	f_c^* at $\tau = 50$[a]
a	0°	11.46	2–3	τ:	2.0	2.32	2.83	3.78	6.55	13.3	0.0495
b	30°	10.89	2–3	τ:	2.0	2.48	3.25	4.8	10.2	33.4	0.0874
c	60°	7.17	2–3	τ:	2.0	2.55	3.55	5.75	15.5	–	0.125
d	75°	3.93	2–3	τ:	2.0	2.58	3.58	5.77	15.4	–	0.124

[a] The last column represents the cloud fraction f_c^* appropriate for $\tau = 50$.

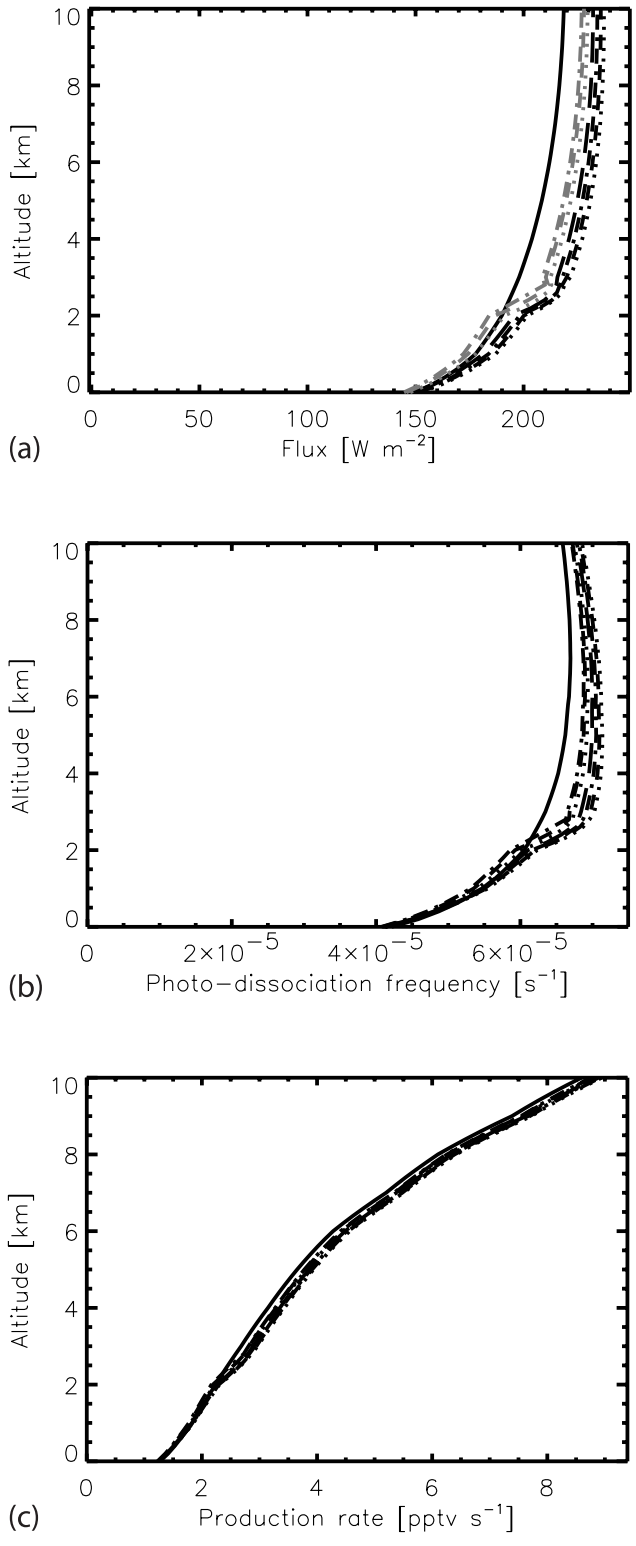

Figure 3. (a) Actinic flux profile, (b) photodissociation frequency profile of $O_3 \rightarrow O(^1D)$, and (c) production rate profile of $O(^1D)$. The cloud is positioned between 2 and 3 km. The SZA = 0°. The solid line is clear sky; the other lines are for the cloud combinations given in Table 2 for case a.

[36] One of the most noticable things is the difference in shape of the actinic flux and $O(^1D)$ production rate compared with the OH production rate in the lowest 10 km of the troposphere: the first two have minima at the surface and increase with altitude, while the latter has a local maximum near the surface and then decreases with altitude. This behavior can be explained by reminding that OH production is dependent on the O_3 concentration for production of $O(^1D)$, the H_2O concentration as a species taking part in the reaction to produce OH, and the O_2 and N_2 concentrations acting as an alternative sink for $O(^1D)$ that compete with the H_2O reaction (see equations (6) and (7)). Because the water vapor concentration decreases strongly with height in the lowest 15 km of the atmosphere, in this region this is the limiting factor for the OH production.

[37] Figures 4a and 4c indicate that most of the OH in the troposphere is produced in the lower part, with the maximum in the lowest few kilometers and a second local maximum just above the cloud top. Depending on the SZA, the production rate of OH at surface level in mid-latitude summer situations varies between 0.3 pptv s^{-1} for SZA = 0° and 0.06 pptv s^{-1} for SZA = 75° and at 10 km between 0.03 pptv s^{-1} and 0.007 pptv s^{-1}, respectively. Above the tropopause there is an even higher maximum in the OH production of 1.45 pptv s^{-1} for SZA = 0° and 0.75 pptv s^{-1} for SZA = 75° between 45 and 55 km. The maximum in the stratosphere as a mixing ratio may be high; the absolute production rate in molecules per second per volume unit at high altitudes is much smaller than at the surface. Differences in production between various cloud situations are minimal at high altitudes, and because we have restricted this study to the troposphere, we will not take the higher atmospheric levels into account.

[38] The small discontinuities in the shape of the production profiles in the figures above the clouds have no physical origin but come from the 1 km resolution of the input gas and temperature profiles. Near the surface the production rate of OH is slowly decreasing which is caused by the low surface albedo ($\alpha_s = 0.05$) that absorbs much of the direct and multiple scattered radiation.

[39] In order to estimate the impact on the calculated OH production (P(OH)) when clouds are scaled, we compare the production profiles of a set of solutions i that follow an isoline of radiance in Figure 2 with the combination ($\tau = 50$, f_c*), which is our optically thick reference cloud (called "thick cloud combination" in the next sections) in Figures 4b and 4d. These figures show the percent differences of individual combinations $P(\mathrm{OH})_i$ to the thick cloud situation: $((P(\mathrm{OH})_i - P(\mathrm{OH})_{\mathrm{thick}})/P(\mathrm{OH})_{\mathrm{thick}}) \times 100\%$. Owing to the very small cloud fraction and consequently the large cloud-free part of the thick cloud combination, it is not difficult to understand that this combination is closest to the clear sky situation in most photochemical aspects simply because the weight of the clear sky is largest (conform equation (4)). A figure for the percent difference of ozone photodissociation frequency $j(O_3)$ is exactly the same as for P(OH) because the production of OH is a multiplication of the dissociation frequency with locally constant factors of concentrations and the branching ratio f_{H_2O}.

[40] The production rates of OH above a cloud are always higher compared with the thick cloud situation

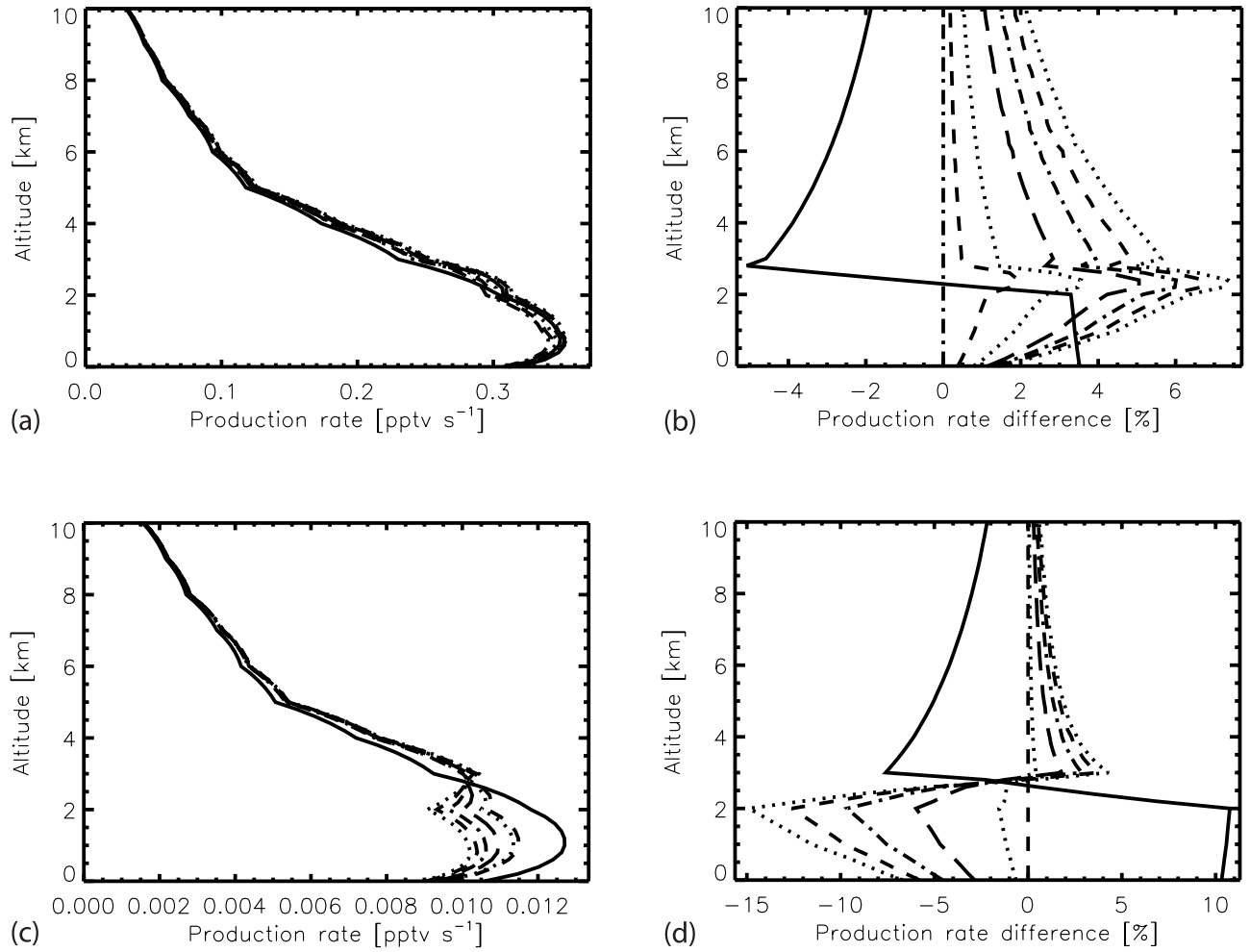

Figure 4. (a) The primary production rate of OH (b) and the difference in primary production rate of OH relative to the thick cloud combination (τ = 50, f_c*) for SZA = 0° (case a, top) and 75° (case *d*, bottom). The solid line represents clear sky; in Figures 4b and 4d the straight vertical dashed line is the thick cloud combination and the other lines indicate the other cloud combinations given in Table 2.

independent of the SZA because of the extra radiation scattered upward by the cloud. The relative amount of increase in production just above the cloud for an optically thin layer (τ = 2.0) is between +5% for SZA = 0° to +4% for SZA = 75° and reduces for combinations (τ, f_c) with a thicker cloud. The positive difference for a thin cloud compared with the thick cloud combination actually means an underestimation of the produced OH in case the effective cloud fraction of a thick cloud is assumed where the actual cloud is thin.

[41] In the cloud the production rate of OH changes abruptly. Owing to the heavily increased scattering by non-absorbing particles that increase the amount of light, the production rate increases by a few percent and then decreases again until the cloud bottom. The altitude of the maximum increase compared with a thick cloud rises with increasing SZA. For SZA = 0° this maximum is located halfway the 1 km thick cloud layer, but for SZA = 75° this maximum is located very close to the cloud top. In-cloud errors for the thin cloud combination (τ = 2, f_c = 1) can locally be as large as +7% for SZA = 0° and ranges from +4% to −15% for SZA = 75°. Combinations of small SZA and optically thin clouds (τ < 5) have a primary OH production rate that stays above the clear sky values throughout the cloud, while combinations with a higher optical thickness end up with lower production rate than clear sky at the bottom of the cloud. Note that the sequence of the profiles has changed.

[42] At the surface all combinations (τ, f_c) have a lower production than clear sky, and the difference with a thick cloud depends on the SZA and the cloud fraction due to the blocking of the direct sunlight component by clouds and the larger optical path with more scattering that reduces the contribution to the actinic flux. The difference in OH production for the thinnest cloud combination (τ = 2, f_c = 1) relative to the thick cloud combination is between +1.5% and +0.5% for SZA = 0° and SZA = 30° but is negative to −7% and −6% at SZA = 60° and SZA = 75°, respectively; this difference is decreasing (in absolute sense) for thicker cloud combinations.

4.3. Total Tropospheric OH Production

[43] The total tropospheric production of OH (in a column) is calculated by vertically integrating the production in

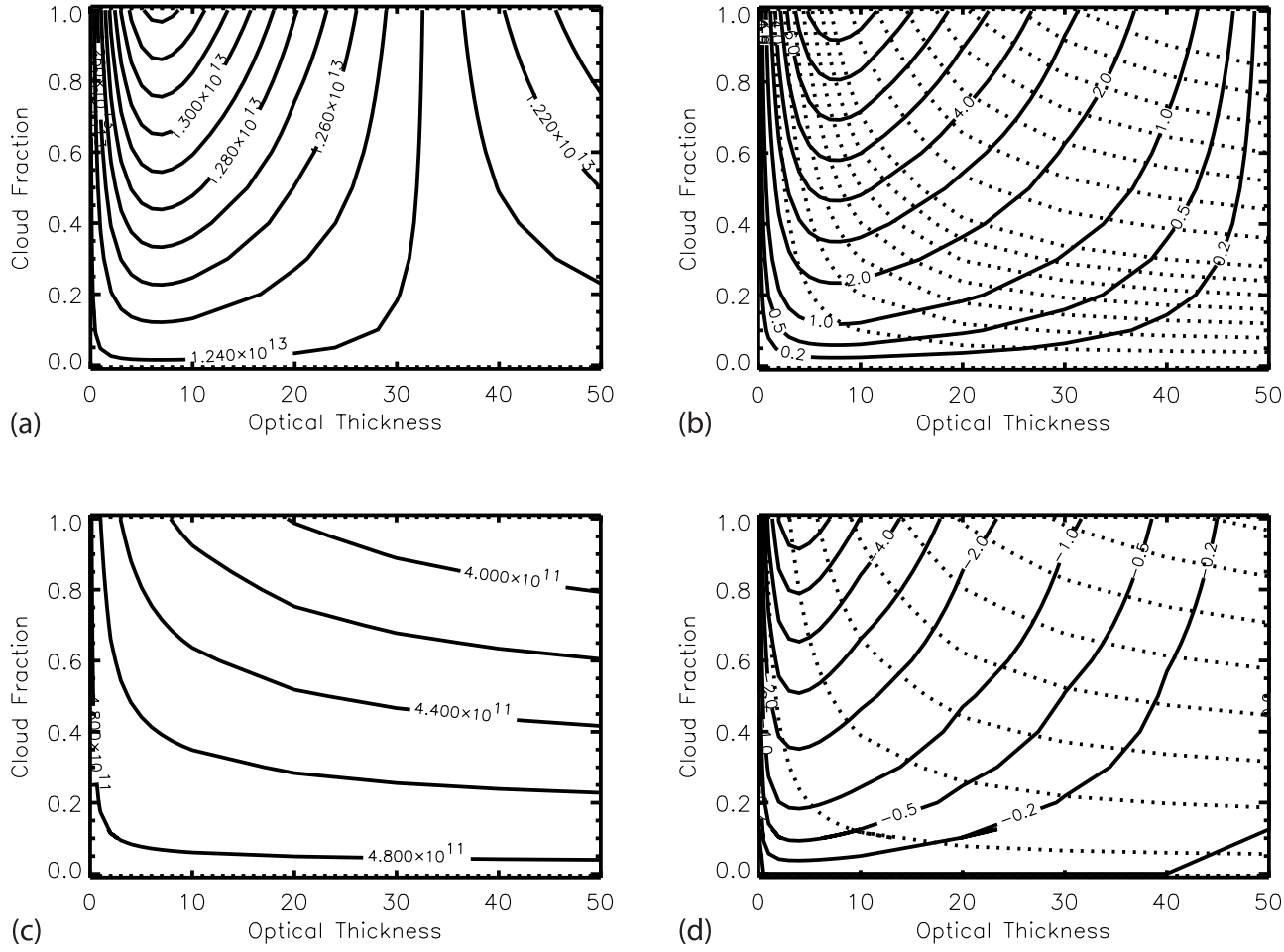

Figure 5. (a) Total tropospheric column production rate of OH (cm^{-2} s^{-1}) from 0 to 10 km for combinations of cloud fractions and optical thicknesses and (b) the difference to the corresponding thick cloud situation in percent for a SZA = 0° (case a, top) and 75° (case d, bottom). The cloud is located between 2 and 3 km. The dotted lines in Figures 5b and 5d indicate the same isolines of wavelength-integrated radiance as in Figure 2.

the layers. Although the tropopause varies in height from a low altitude at the poles to a higher altitude at the equator, we have chosen to restrict the ''troposphere'' in our case to the lowest 10 km of the atmosphere. These total production values are shown in Figures 5a and 5c. Although the cloud fraction and the optical thickness vary over their complete range ($f_c = 0.0-1.0$ and $\tau = 0.0-50.0$, respectively), the total primary OH production of the tropospheric column stays in the same order of magnitude for the same SZA. The maximum for SZA = 0° is 1.33×10^{13} cm^{-2} s^{-1} and for SZA = 75° is 4.8×10^{11} cm^{-2} s^{-1}, respectively.

[44] The impact of the scaling of clouds to an effective cloud fraction on the primary OH production is calculated when we take the relative difference in percent to the corresponding thick cloud situation ($\tau = 50$, f_c*), as shown in Figures 5b and 5d. To indicate which sets of solutions are compared with what thick cloud combination, dotted lines of equal I* at TOA are plotted as guides (equal to Figure 2).

[45] In Figures 5b and 5d one can see that for small SZA, the total column OH production relative to thick clouds is positive, which again indicates an underestimation for clouds scaled to an effective cloud fraction. The positive difference decreases with increasing SZA to a point where the effect of clouds on the total column production of OH turns negative for SZA < 45°, like shown in the plot for case d.

[46] The maximum impact on the column OH production is shown in Figure 6, where the thinnest cloud solution ($\tau, f_c = 1.0$) is plotted against the cloud fraction for a cloud with optical thickness $\tau = 50$. For small SZA the differences between the total atmospheric OH production column (up to 80 km) and the tropospheric column are negligible, but for larger SZA this relative total atmospheric column difference is up to 1% smaller (for SZA = 75° the maximum atmospheric difference is −5.5% while the tropospheric column difference is −6.5%).

[47] Figure 7 shows the maximum relative OH primary production differences to a thick cloud at certain levels in the atmosphere: at surface level (0 km), just below the cloud (at 1.8 km), halfway the cloud (2.6 km), and just above the cloud (3.2 km). From these plots it is possible to estimate what the contribution of certain layers to the differences in the total OH column production is. A positive total tropospheric OH production column differ-

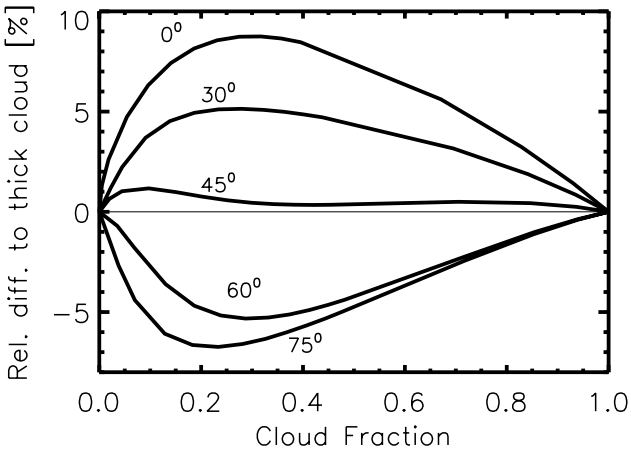

Figure 6. Maximal relative difference of the total tropospheric column OH primary production against the cloud fraction f^* for a cloud with $\tau = 50$ and different values of the solar zenith angle (shown in the plot). The cloud is located between 2 and 3 km.

ence for small SZA is caused by the sum of the increased production above, at, and below the cloud, while the negative total tropospheric column differences for larger SZA are caused by the strong reduction below the cloud that overcompensates a lower positive difference above the cloud (net less production).

4.4. Other Concentration Profiles

[48] To study the effect of other ozone, water vapor, and temperature profiles on the primary OH production, we did calculations with the tropical profile set instead of midlatitude summer profile. These calculations were for clouds between 2 and 3 km and the sun in zenith (SZA = 0°). The ozone column remained fixed to 300 DU, in order to get the same amount of UV radiation into the troposphere for a fair comparison.

[49] Owing to the increased water vapor content in the tropics, there is generally also more primary OH production; at the surface there are 0.4 pptv s^{-1} for tropical concentration profiles compared with 0.3 pptv s^{-1} for the midlatitude summer profile set. The local maximum in OH

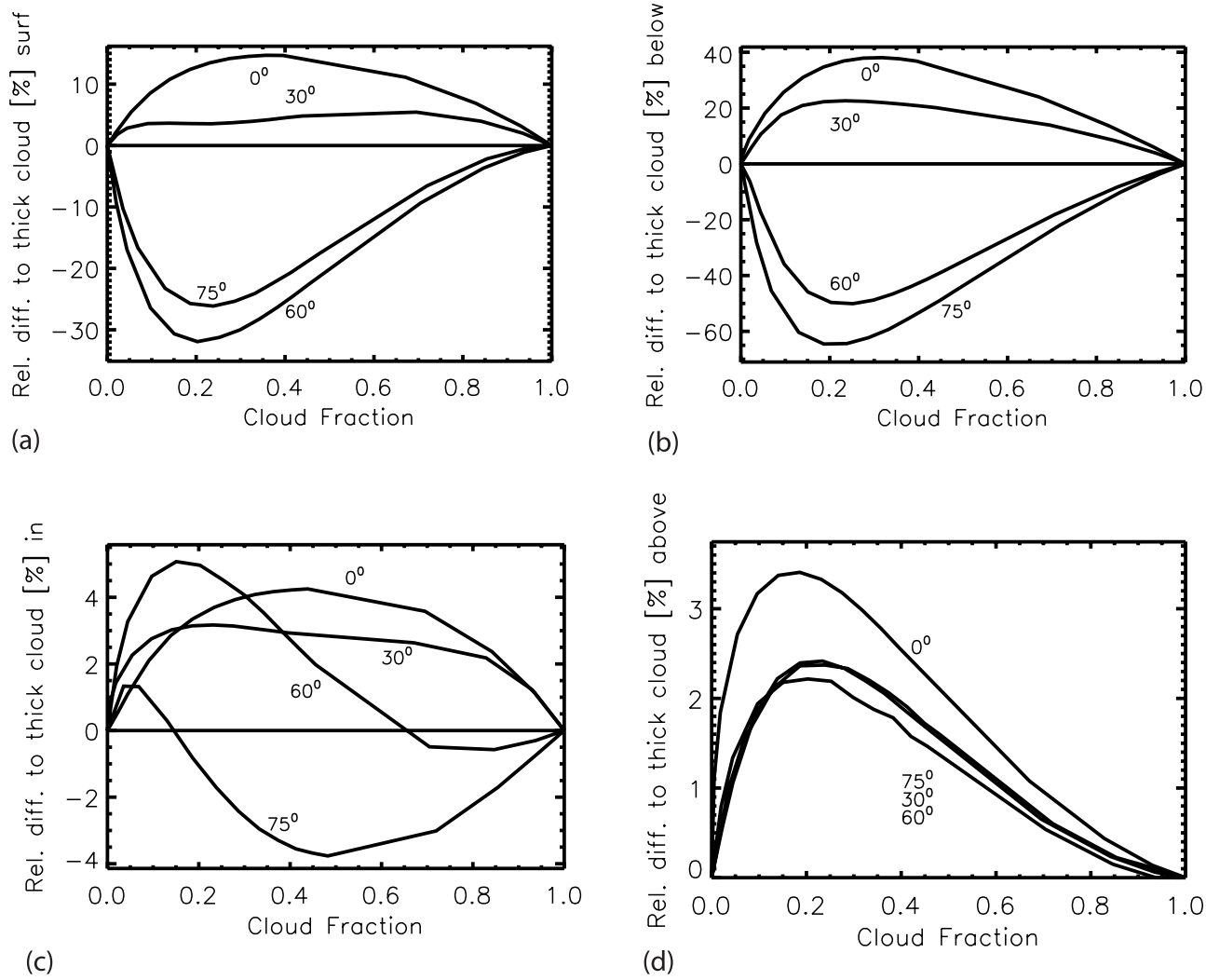

Figure 7. Maximal relative difference of the OH primary production against the cloud fraction f^* for (a) a cloud with $\tau = 50$ at the surface (0 km), (b) just below a cloud (at 1.8 km), (c) in the cloud (at 2.6 km), and (d) just above the cloud (at 3.2 km). The values of the solar zenith angles are shown in the plot.

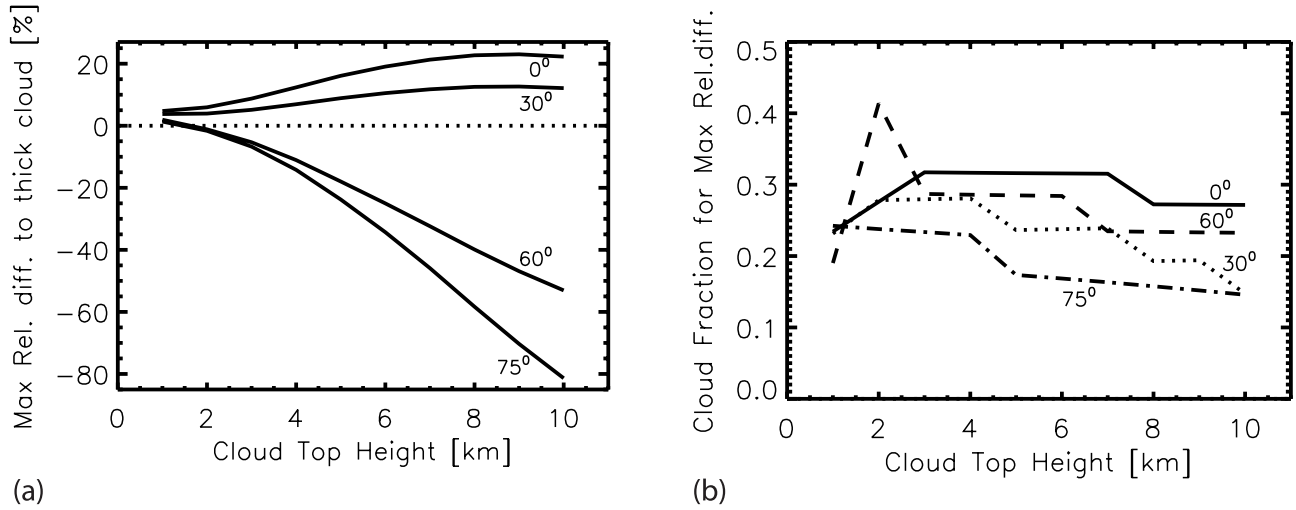

Figure 8. (a) Maximum relative difference of the tropospheric column OH primary production against the cloud top height for a cloud with $\tau = 50$ and a 1 km geometrical thickness. (b) The cloud fraction for which the maximum relative difference occurs for the same cloud as shown in Figure 8a. The values of the solar zenith angles are shown in the plot.

production just above the cloud in midlatitude summer cases has disappeared in the tropical case. The local relative difference to thick clouds in the tropical case is slightly reduced throughout the atmosphere. This reduction is maximally 0.5% at the cloud for low optical thicknesses. Above or below the cloud, the local differences relative to a thick cloud are within ±0.2% compared with their similar midlatitude summer profiles. The small difference is due to a weak dependence of the ozone photolysis frequency on the ozone profile when the ozone column is kept constant.

4.5. Varying the Cloud Altitude

[50] We looked at clouds at an altitude between 4 and 5 km, with the same geometrical thickness as in the earlier sections (a layer of 1 km thickness) but with cloud combinations (τ, f_c) adjusted for an equal radiance at TOA. A comparison of the absolute primary OH production shows no significant local absolute difference at altitudes above 5 km compared with a cloud between 2 and 3 km. The local relative OH production difference compared with a thick cloud combination increases at and below the cloud for all SZA compared with the lower clouds (positive for SZA = 0° and SZA = 30° and in negative direction for SZA = 60° and SZA = 75°). The maximum of production difference for ($\tau = 2$, $f_c = 1.0$) and SZA = 0° in the cloud is now +9% compared with +7% for clouds between 2 and 3 km, and the maximum negative difference at the cloud bottom for SZA = 75° is −20% compared with −15% for clouds at 2 and 3 km. It was found that differences of total tropospheric column production relative to thick clouds for a cloud at 4–5 km increase in positive direction to +14% and +7.5% for SZA = 0° and SZA = 30° and in negative direction to −15% and −18% for SZA = 60° and SZA = 75°.

[51] The maximum impact of the cloud top height on total tropospheric OH primary production is shown in Figure 8. In this plot the maximum column difference relative to a thick cloud combination is plotted against the cloud top height. The difference between small and large SZA is quite clear: For small SZA the difference increases in the positive direction with an increasing cloud top height (meaning an increasing underestimation of primary OH production with a higher cloud top), but for larger SZA the difference increases strongly in the negative direction for an increasing cloud top height (thus meaning an overestimation of production in the thick cloud case).

4.6. NO_2 Photodissociation

[52] The wavelength range at which NO_2 absorbs photons for photodissociation extends to longer wavelengths than O_3 (up to 425 nm for NO_2 compared with 360 nm for O_3). The stronger solar irradiation at these longer wavelengths and the reduced Rayleigh scattering bring more light into the lower troposphere, and thus the photodissociation frequency of nitrogen dioxide $j(NO_2)$ is larger than for ozone. The differences in photodissociation frequency of NO_2, or the production of NO + O(^3P), relative to the standard thick cloud combination of $\tau = 50$ are shown in Figure 9, which can be compared with those of ozone (in Figure 4).

[53] In general, the difference profiles behave the same as the ozone difference profiles. Above the cloud the difference to a thick cloud is always positive, and in and below the cloud this difference turns negative with increasing SZA. One notes, however, that the differences for NO_2 are larger than for O_3. Above the cloud the NO_2 photodissociation differences reduce considerably slower with increasing altitude than the ozone differences profiles: While the difference for the combination ($\tau = 2$, $f_c = 1$) for SZA = 0° just above the cloud is roughly the same (+5%), at 10 km altitude the difference for the same combination is +4% for NO_2 while it was +2% for OH (which is the same as for O_3). The maximum for ($\tau = 2$, $f_c = 1$) and SZA = 0° in and just below the cloud is +9% for NO_2 while it is +7% for OH. As a negative maximum there is −35% for NO_2 while there is −14% for OH for ($\tau = 2$, $f_c = 1$) and SZA = 75° just below the cloud.

[54] Figure 10 shows the maximum difference for the total tropospheric column NO_2 photodissociation to a thick cloud against the cloud fraction for a cloud between 2 and 3

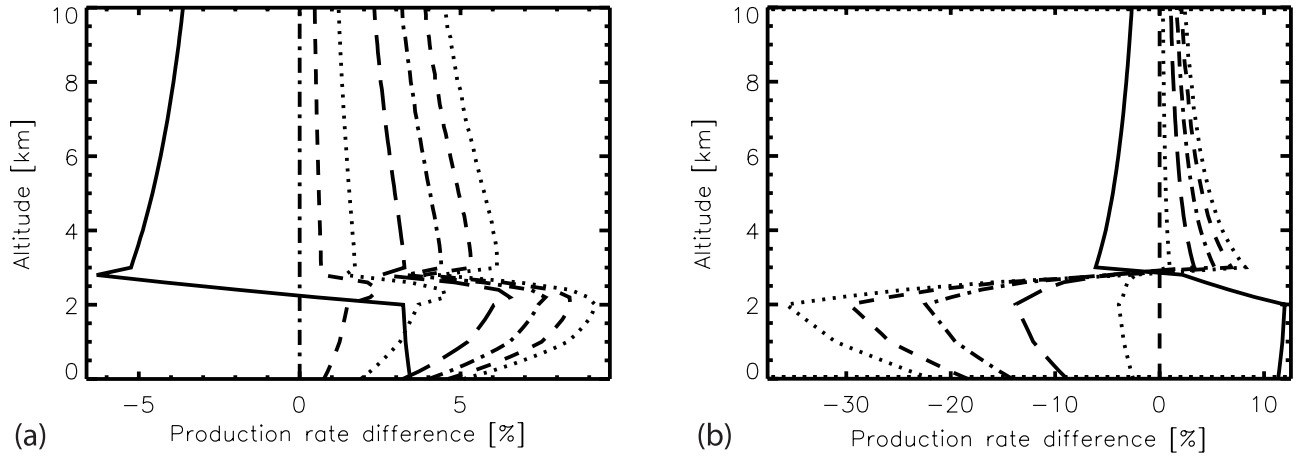

Figure 9. The difference in photodissociation of $NO_2 \rightarrow NO + O(^3P)$ relative to the thick cloud case ($\tau = 50$, f_c*) for (a) SZA = 0° (case a) and (b) SZA = 75° (case d). The cloud is positioned between 2 and 3 km. The solid line represents clear sky; the vertical dashed line is the thick cloud situation. The other lines are the cloud combinations mentioned for the two cases in Table 2.

km (compare Figure 6). The maximum total tropospheric column NO_2 photodissociation difference relative to a thick cloud shows that although the local differences in NO_2 photodissociation are larger, the total column differences do not increase with an equal amount. The maximum difference for SZA = 0° and SZA = 30° are +6.7% and +4.7% respectively. The maximum difference for SZA = 45° is +3%, and this SZA is not near the turning point from positive to negative column differences like for OH. The maximum column differences for SZA = 60° are partly positive for cloud fractions $f_c < 0.2$ and negative for larger cloud fractions (maximum +0.5% and −1%, respectively). For SZA = 75° the tropospheric column differences are negative for all cloud fractions (maximum −3.5%).

[55] From the results above we conclude that scaling of clouds to effective cloud fractions has locally (with respect to altitude) larger impact on NO_2 photodissociation than on O_3 photodissociation and OH production, but for column differences the values are less than for OH.

5. Conclusions

[56] In this paper we have studied the impact on the photodissociation rate of O_3 and NO_2 and primary production of OH of the scaling of actual clouds to an effective cloud with a high optical thickness and an appropriate cloud fraction ($\tau = 50$, f_c*) that gives the same upward radiance from nadir at the top of the atmosphere (TOA). We have shown that for selected cloud solutions (τ, f_c) located between 2 and 3 km that have the same upward radiance at TOA, local differences in the vertical OH production profile or O_3 photodissociation profile attained values ranging between +7% for small solar zenith angles (SZA) to −15% for large SZA when compared with the thick cloud combination. For clouds located at higher altitudes this local (with respect to the cloud) difference increases. Positive differences of unscaled cloud combinations compared with the thick cloud combination correspond to an underestimation of the calculated OH production when the retrieved parameters (effective thick clouds) are used for straightforward production calculations.

[57] A vertically integrated tropospheric primary OH production difference compared with a thick cloud between 2 and 3 km indicated that the total difference can attain values of +9% for SZA = 0° to −6.5% for SZA = 75° when the actual clouds are scaled to the combination ($\tau = 50$, $0.1 < f_c^* < 0.5$). When cloud layers are located at a higher altitude between 4 and 5 km, the column differences in OH production become larger, up to +14% and −18% for SZA = 0° and SZA = 75°, respectively. In the cases where the column net primary OH production difference is negative compared with at thick cloud, the strongly reduced production in and below the cloud is not compensated by the net positive production above the cloud layer.

[58] We showed that the column OH production difference to a thick cloud is dependent on the given cloud top. For small solar zenith angles (SZA) this column OH production difference is positive to max +22% for the sun in zenith (indicating an underestimation), while for large SZA this

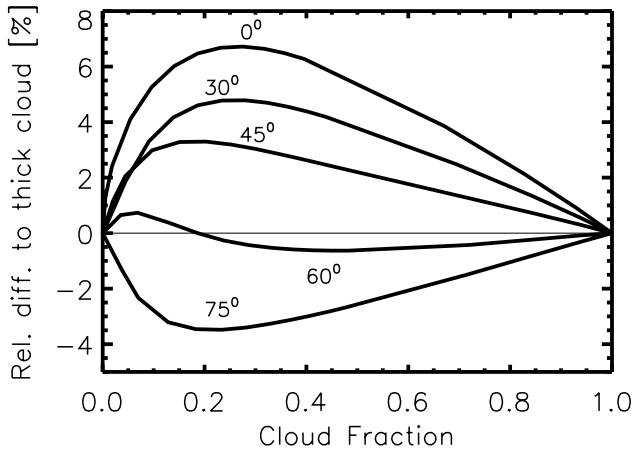

Figure 10. Maximal relative difference of the total tropospheric column NO_2 photodissociation against the cloud fraction f* for a cloud with $\tau = 50$ and different values of the solar zenith angle (shown in the plot). The cloud was located between 2 and 3 km.

difference is strongly negative with increasing cloud top to −81% for SZA = 75°. With respect to NO_2 photodissociation we found that the scaling of clouds to an effective cloud fraction has more influence on local NO_2 photodissociation than on local O_3 photodissociation, but for the tropospheric column difference this influence is less prominent.

[59] Finally, we conclude that total tropospheric O_3 and NO_2 photodissociation and primary OH production can be determined with reasonable accuracy within 20% using satellite-derived effective cloud fractions for moderate SZA, but in cases of high clouds in combination with large SZA the use of effective cloud fractions can lead to unacceptably high errors.

[60] **Acknowledgments.** The authors wish to thank NWO/SRON for the financial support of this project.

References

Anderson, G., S. Clough, F. Kneizys, J. Chetwynd, and E. Shettle, AFGL atmospheric constituent profiles, *Tech. Rep. AFGL-TR-86-0110*, Air Force Geophys. Lab., Bedford, Mass., 1986.

Burrows, J., et al., Global Ozone Monitoring Experiment (GOME): Mission concept and first scientific results, *J. Atmos. Sci.*, *56*, 151–175, 1999.

Cahalan, R., W. Ridgeway, W. Wiscombe, T. Bell, and J. Snider, The albedo of fractal stratocumulus clouds, *J. Atmos. Sci.*, *51*, 2434–2455, 1994.

Casadio, S., C. Zehner, G. Poscane, and E. Putz, Empirical retrieval of the atmosphic air mass factor (ERA) for the measurement of water vapour vertical content using GOME data, *Geophys. Res. Lett.*, *27*, 1483–1486, 2000.

de Winter-Sorkina, R., Tropospheric OH primary production from ERS-2 data, in *Proceedings of the ERS-ENVISAT Symposium*, *ESA, SP-461*, Eur. Space Agency, Noordwijk, Netherlands, 2000.

de Winter-Sorkina, R., and O. Tuinder, Estimation of tropospheric photodissociation rates and surface UV from GOME measurements, in *Proceedings of ESAMS'99—European Symposium on Atmospheric Measurements from Space*, *ESA, WPP-161*, vol. 2, pp. 555–561, European Space Agency, Noordwijk, Netherlands, 1999.

Eisele, F., and D. Tanner, Ion-assisted tropospheric OH measurements, *J. Geophys. Res.*, *96*, 9295, 1991.

Elterman, L., UV, visible, IR attenuation for altitudes to 50 km, *Tech. Rep. AFCRL-68-0153*, *285*, Air Force Res. Lab., Cambridge, Mass., 1968.

Gardner, E., P. Sperry, and J. Calvert, Primary quantum yields of NO_2 photodissociation, *J. Geophys. Res.*, *92*, 6642–6652, 1987.

Goody, R., and Y. Yung, *Atmospheric Radiation; Theoretical Basis*, 2nd ed., Oxford Univ. Press, New York, 1989.

Hard, T., R. O'brien, C. Chan, and A. Mehrabzadeh, Tropospheric free radical determination by FAGE, *Environ. Sci. Technol.*, *18*, 768–777, 1984.

Hoogen, R., V. Rozanov, and J. Burrows, Ozone profiles from GOME satellite data: Algorithm description and first validation, *J. Geophys. Res.*, *104*, 8263–8280, 1999.

Koelemeijer, R., and P. Stammes, Effects of clouds on ozone column retrieval from GOME UV measurements, *J. Geophys. Res.*, *104*, 8281–8294, 1999.

Koelemeijer, R., and P. Stammes, A fast method for retrieval of cloud parameters using oxygen A-band measurements from the Global Ozone Monitoring Experiment, *J. Geophys. Res.*, *106*, 3475–3490, 2001.

Krol, M., P. van Leeuwen, and J. Lelieveld, Global OH trend inferred from methylchloroform measurements, *J. Geophys. Res.*, *103*, 10,697–10,711, 1998.

Krol, M., P. van Leeuwen, and J. Lelieveld, Reply, *J. Geophys. Res.*, *106*, 23,159–23,164, 2001.

Kurosu, T., K. Chance, and R. Spurr, CRAG—Cloud Retrieval Algorithm for the European Space Agency's Global Ozone Monitoring Experiment, paper WWP-161 presented at European Symposium on Atmospheric Measurements from Space (ESAMS '99), pp. 513–521, Eur. Space Agency, Noordwijk, Netherlands, 1999.

Kuze, A., and K. Chance, Analysis of cloud top height and cloud coverage from satellites using the O_2 A and B bands, *J. Geophys. Res.*, *99*, 14,481–14,491, 1994.

Lambert, J.-C., et al., Combined characterisation of GOME and TOMS total ozone measurements from space using ground-based observations from the NDSC, *Adv. Space Res.*, *26*, 1931–1940, 2000.

Levy, H., II, Normal atmosphere: Large radical and formaldehyde concentrations predicted, *Science*, *173*, 141–143, 1971.

Liou, K., *An Introduction to Atmospheric Radiation*, Academic, San Diego, Calif., 1980.

Liou, K., *Radiation and Cloud Processes in the Atmosphere: Theory, Observing and Modeling*, Oxford Univ. Press, New York, 1992.

Los, A., M. van Weele, and P. Duynkerke, Actinic fluxes in broken cloud fields, *J. Geophys. Res.*, *102*, 4257–4266, 1997.

Loyola, D., A new cloud recognition algorithm for optical sensors, paper presented at International Geoscience and Remote Sensing Symposium, pp. 572–574, Inst. of Electr. and Electron, Eng., Seattle, Wash., 1998.

Madronich, S., and S. Flocke, *The Role of Solar Radiation in Atmospheric Chemistry*, pp. 1–26, Springer-Verlag, New York, 1998.

Madronich, S., and G. Weller, Numerical integration errors in calculated tropospheric photodissociation rate coefficients, *J. Atmos. Chem.*, *10*, 289–300, 1990.

Marshak, A., A. Davis, W. Wiscombe, and R. Calahan, Radiative smoothing in fractal clouds, *J. Geophys. Res.*, *100*, 26,247–26,261, 1995.

Maurellis, A., R. Lang, W. van der Zande, I. Aben, and W. Ubachs, Precipitable water column retrieval from GOME data, *Geophys. Res. Lett.*, *27*, 903–906, 2000.

Mount, G., The measurement of tropospheric OH by long-path absorption, 1, Instrumentation, *J. Geophys. Res.*, *97*, 2427–2444, 1992.

Munro, R., R. Siddans, W. Reburn, and B. Kerridge, Direct measurement of tropospheric ozone distributions from space, *Nature*, *392*, 168–171, 1998.

Noel, S., M. Buchwitz, H. Bovensmann, R. Hoogen, and J. Burrows, Atmospheric water vapour amounts retrieved from GOME satellite data, *Geophys. Res. Lett.*, *26*, 1841–1844, 1999.

Prinn, R., and J. Huang, Comment on "Global OH trend inferred from methylchloroform measurements" by Maarten Krol et al., *J. Geophys. Res.*, *106*, 23,151–23,157, 2001.

Prinn, R., R. Weiss, B. Miller, J. Huang, F. Alya, D. Cunnold, P. Fraser, D. Hartley, and P. Simmonds, Atmospheric trends and lifetime of CH_3CCL_3 and global OH concentrations, *Science*, *269*, 189–190, 1995.

Prinn, R., et al., Evidence for substantial variations of atmospheric hydroxyl radicals in the past two decades, *Science*, *292*, 1882–1888, 2001.

Sander, S., et al., Chemical kinetics and photochemical data for use in stratospheric modelling—Supplement to evaluation 12: Update of key reactions, *Tech. Rep. 13*, Jet Propul. Lab., Pasadena, Calif., 2000.

Seinfeld, J., and S. Pandis, *Atmospheric Chemistry and Physics*, John Wiley, New York, 1998.

Siddans, R., B. Kerridge, A. Stevens, and R. Munro, Height resolved ozone retrievals spanning the troposphere and stratosphere for GOME, in *Proceedings of ESAMS'99—European Symposium on Atmospheric Measurements from Space, ESA*, *WPP-161*, pp. 299–305, Eur. Space Agency, Noordwijk, Netherlands, 1999.

Stamnes, K., S. Tsay, W. Wiscombe, and K. Jayaweera, A numerically stable algorithm for discrete-ordinate-method radiative transfer in multiple scattering and emitting layered media, *Appl. Opt.*, *27*, 2502–2509, 1988.

Tuinder, O. N. E., R. de Winter-Sorkina, and P. J. H. Builtjes, Retrieval methods of effective cloud cover for the GOME instrument: An intercomparison, *Atmos. Chem. Phys. Discuss.*, *2*, 623–668, 2002.

van der A, R., R. van Oss, and H. Kelder, Ozone profile retrieval from GOME data, in *Remote Sensing of Clouds and the Atmosphere III, Proceedings of SPIE* vol. 3495, edited by J. Russell, pp. 221–229, Int. Soc. for Opt. Eng., Bellingham, Wash., 1998.

van Weele, M., Estimation of global tropospheric OH-production using satelliteborne observations of photodissociation rates, *Tech. Rep. 97-6*, Inst. for Mar. and Atmos. Res., Utrect, Netherlands, 1997.

van Weele, M., and P. Duynkerke, Effects of clouds on the photodissociation of NO_2: Observations and modelling, *J. Atmos. Chem.*, *16*, 231–255, 1993.

von Bargen, A., T. Kurosu, K. Chance, D. Loyola, B. Aberle, and R. Spurr, ERS-2, Cloud Retrieval Algorithm for GOME (CRAG), final technical report, Smithsonian Astrophys. Obs., Cambridge, Mass., 2000.

Warneck, P., *Chemistry of the Natural Atmosphere*, Academic, San Diego, Calif., 1988.

P. J. H. Builtjes and O. N. E. Tuinder, Institute for Marine and Atmospheric Research Utrecht (IMAU), Utrecht University, P.O. Box 80005, 3508 TA, Utrecht, Netherlands. (builtjes@phys.uu.nl; tuinder@phys.uu.nl)

R. de Winter-Sorkina, National Institute for Public Health and the Environment (RIVM), P.O. Box 1, 3720 BA, Bilthoven, Netherlands. (winter@phys.uu.nl)